AGU PUBLICATIONS

Water Resources Research

RESEARCH ARTICLE

10.1002/2014WR016019

Microbubble transport in water-saturated porous media

Y. Ma[1,2], X.-Z. Kong[1,3], A. Scheuermann[1,4], S. A. Galindo-Torres[1,4], D. Bringemeier[1,5], and L. Li[1,2]

[1]Research Group on Complex Processes in Geo-Systems, School of Civil Engineering, University of Queensland, Brisbane, Queensland, Australia, [2]State Key Laboratory of Hydrology-Water Resources and Hydraulic Engineering, Hohai University, Nanjing, China, [3]Institute of Geophysics, ETH-Zurich, Zurich, Switzerland, [4]Geotechnical Engineering Centre, University of Queensland, Brisbane, Queensland, Australia, [5]Golder Associates (Australia) Pty Ltd., Brisbane, Queensland, Australia

Abstract Laboratory experiments were conducted to investigate flow of discrete microbubbles through a water-saturated porous medium. During the experiments, bubbles, released from a diffuser, moved upward through a quasi-2-D flume filled with transparent water-based gelbeads and formed a distinct plume that could be well registered by a calibrated camera. Outflowing bubbles were collected on the top of the flume using volumetric burettes for flux measurements. We quantified the scaling behaviors between the gas (bubble) release rates and various characteristic parameters of the bubble plume, including plume tip velocity, plume width, and breakthrough time of the plume front. The experiments also revealed circulations of ambient pore water induced by the bubble flow. Based on a simple momentum exchange model, we showed that the relationship between the mean pore water velocity and gas release rate is consistent with the scaling solution for the bubble plume. These findings have important implications for studies of natural gas emission and air sparging, as well as fundamental research on bubble transport in porous media.

Key Points:
- Visualization of bubble migration was enabled by using transparent gelbeads
- Characteristic width of bubble plume following a power law with an exponent of 0.2
- Circulation of pore water velocity following a power law with an exponent of 0.6

Supporting Information:
- Supporting Information S1

Correspondence to:
Y. Ma,
y.ma5@uq.edu.au,
maye0309@gmail.com

Citation:
Ma, Y., X.-Z. Kong, A. Scheuermann, S. A. Galindo-Torres, D. Bringemeier, and L. Li (2015), Microbubble transport in water-saturated porous media, *Water Resour. Res.*, *51*, 4359–4373, doi:10.1002/2014WR016019.

Received 18 JUN 2014
Accepted 17 MAY 2015
Accepted article online 20 MAY 2015
Published online 18 JUN 2015

1. Introduction

Gas transport in porous media is prevalent in many geoenvironmental systems with or without engineering applications: for example, soil remediation using air sparging to clean volatile contaminants [*Ji et al*., 1993], gas leakage through faults/fractures during gas drilling [*Osborn et al*., 2011], enhancement of oil recovery by injecting gas for oil displacement [*Montgomery and Morea*, 2001], coal seam gas extraction in a dewatering process [*Moore*, 2012], natural greenhouse gas emission from river/seabeds [*Santos et al*., 2012], and moffetts and mineral springs [*Weinlich et al*., 1998]. This study focus on transport of gas in the form of discrete microbubbles. In the following, we give an overview of previous work related to different modes of gas transport, including microbubble flow in porous media, in relation to anthropogenic air sparging and natural gas leakage.

1.1. Air Sparging

Subsurface remediation using in situ air sparging has become a widely used technology for remediating sites contaminated by volatile organic materials or heavy metals [*Johnson et al*., 1993; *Pleasant et al*., 2014]. It is well known that the remediation efficiency is primarily affected by the gas flow patterns, which are often categorized as channel flow, slug flow, or bubble flow [*Brooks et al*., 1999; *Chen et al*., 1996; *Elder and Benson*, 1999; *Hu et al*., 2010]. When gas is transported continuously, channel flow may occur. Experiments and numerical simulations have been carried out to investigate the radius of influence area and contaminant removal rate under the condition of channel flow [*Geistlinger et al*., 2009; *Forsyth*, 1993; *Forsyth and Shao*, 1991; *McCray*, 2000; *Thomson and Johnson*, 2000]. However, gas channels might not be necessarily stable. They can migrate [*Kong et al*., 2009, 2010a] or collapse [*Kong et al*., 2010a, 2010b; *Selker et al*., 2007] due to competitions between gas inertias and surface tensions.

When gas channels are not stable, i.e., gas is not transported continuously, slug flow may occur. For example, slug (marcobubbles) flow was found in 2-D etched glass Hele-Shaw cells, where gas bubbles present irregular and ramified shapes [*Li and Yortsos*, 1995]. In the slug flow, bubbles coalesce easily and get trapped in porous media [*Nelson et al*., 2009]. Thus, slug flow generally tends to return to channelized gas flow [*Enouy et al*., 2011; *Zhao and Ioannidis*, 2011]. Moreover, the trapped gas (slug) would reduce hydraulic

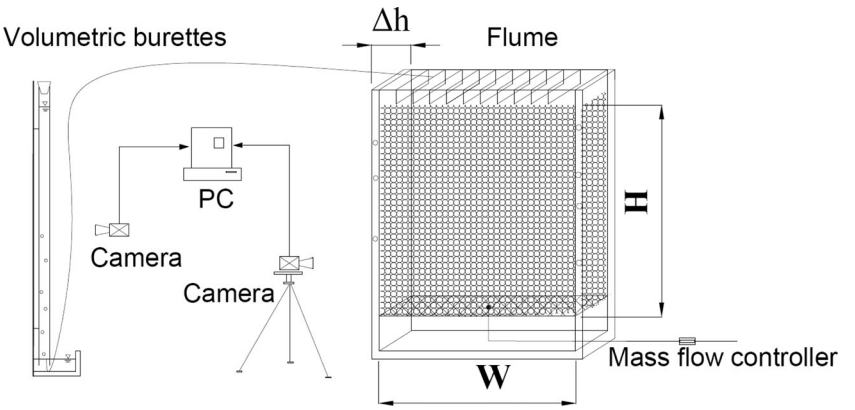

Figure 1. Schematic diagram of the laboratory setup.

conductivity of the porous medium [*Fry et al*., 1997], another drawback of slug flow in the application of air sparging.

Generally speaking, problems associated with air sparging include a limited number of preferential pathways (channelized flow) and small radius of influence area, which in turn constrain biodegradation and remediation [*Hu et al*., 2011]. To overcome some of these limitations, the injection of surfactant-enhanced microbubbles has been considered as an alternative for delivery of supplement oxygen in the subsurface [*Michelsen et al*., 1988]. Microbubbles have larger interfacial area, longer time of presence, and higher concentration in the porous medium. Thus, injection of microbubbles increases the degree of contact between the injected bubbles and the contaminated soil. All these features enhance efficiency in groundwater bioremediation by promoting aerobic conditions for bioreactions and contaminant sorption [*Li et al*., 2014b; *Tsai et al*., 2007]. Furthermore, buoyant rise of the microbubbles may allow them to effectively access regions of

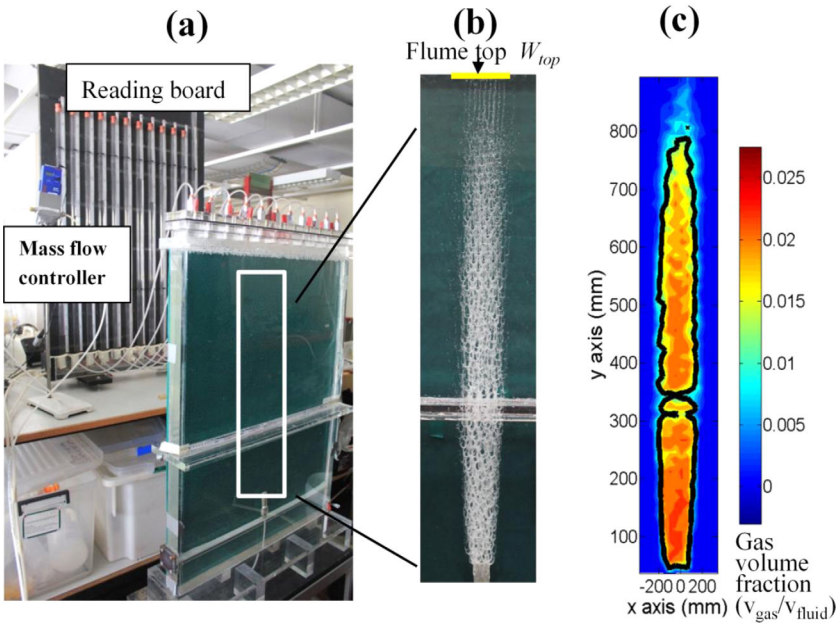

Figure 2. (a) Snapshot of laboratory setup; (b) a typical bubble plume developed before the breakthrough (transient state, $t < t^*$), the plume width (W_{top}) at the flume top was illustrated in yellow line; (c) calculated REV-averaged gas volume fraction distribution based on the bubble plume image shown in Figure 2b, with the solid black line showing the defined edge of the bubble plume. Accordingly, the plume width is the lateral width of the defined edge, and the plume front is the advanced front of the defined edge.

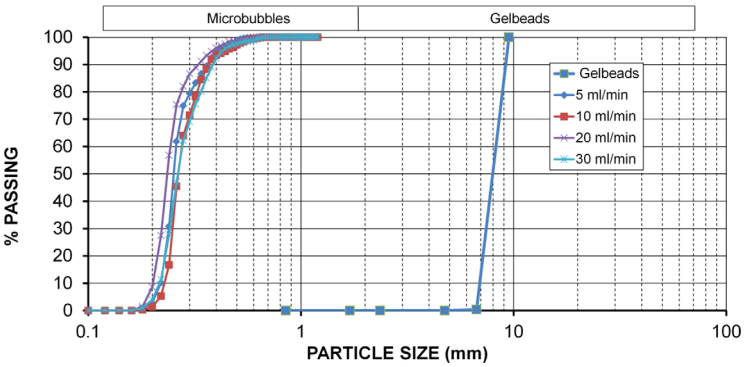

Figure 3. (right) Gelbeads size distribution and (left) bubble size distribution under various gas release rates (size measured in diameter) measured using method in "Size distribution measurement for densely binding bubbles via image analysis" [*Ma et al.*, 2014].

lower permeability [*Wan et al.*, 2001]. In practice, subsurface microbubble injection can be a practical technique with surfactants used to stabilize the microbubbles.

1.2. Gas Leakages

In nature, high concentrations of light hydrocarbon gases (e.g., methane, ethane, and propane), carbon dioxide, and radon have often been found in soils above hydrocarbon gas-bearing rock formations, especially in areas associated with faults zones [*Duddridge et al.*, 1991; *Kemski et al.*, 1992]. These gases, originated from gas-bearing formations, migrate upward through open and connected faults/fractures, producing anomalously high gas concentrations in the upper soil layer.

Anomalies of soil gas concentration observed near the ground surface result from gas transport in the subsurface. The following mechanisms have been proposed for light hydrocarbon gas transport in porous media: (a) diffusion of gas molecules, (b) convective groundwater flow transporting the dissolved gas to the upper soil layer, (c) pressure-driven continuous gas phase transport, and (d) upward movement of discrete microbubbles [*Kristiansson and Malmqvist*, 1984]. Among these mechanisms, diffusion and convective groundwater flow are thought to be relatively slow processes with limited migrating distances [*Fleischer and Mogro-Campero*, 1978, 1979]. Continuous flow of gas occurs when pore space in fractures/soil is continuously occupied by the gas phase of pressure exceeding hydrostatic and capillary pressures, as in geothermal or hydrocarbon-pressurized reservoirs [*Saunders et al.*, 1999]. Given a sufficient amount of gas with adequate pressure gradients, the pressure-driven continuum gas flow could provide a relatively fast gas transport mechanism. *MacElvain* [1969] suggested that gases could also travel buoyantly in the form of discrete microbubbles in order to explain rapid gas transport in areas with no large gas pressure gradients. *D'Arrigo* [1983] provided evidences that largely hydrophobic surfactants stabilize the long-lived gas microbubbles released from forest soils, at unusually high concentrations and with bubble sizes ranging from 0.1 to 100 μm. It is believed that widespread humic acids, acting as surfactants, help to stabilize microbubbles in nature. Bubbles produced naturally through the nucleation process could have much smaller sizes. For example, *Rebata-Landa and Santamarina* [2012] reported bubbles of sizes ranging from 10 to 1000 nm under different bubble nucleation

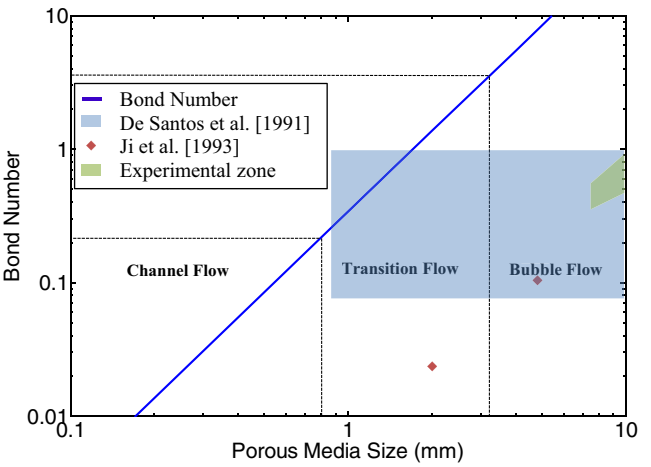

Figure 4. Flow patterns characterized by the pore size of porous media and the Bond number (modified from *Brooks et al.* [1999]). The blue-shaded portion represents data from *De Santos et al.* [1991].

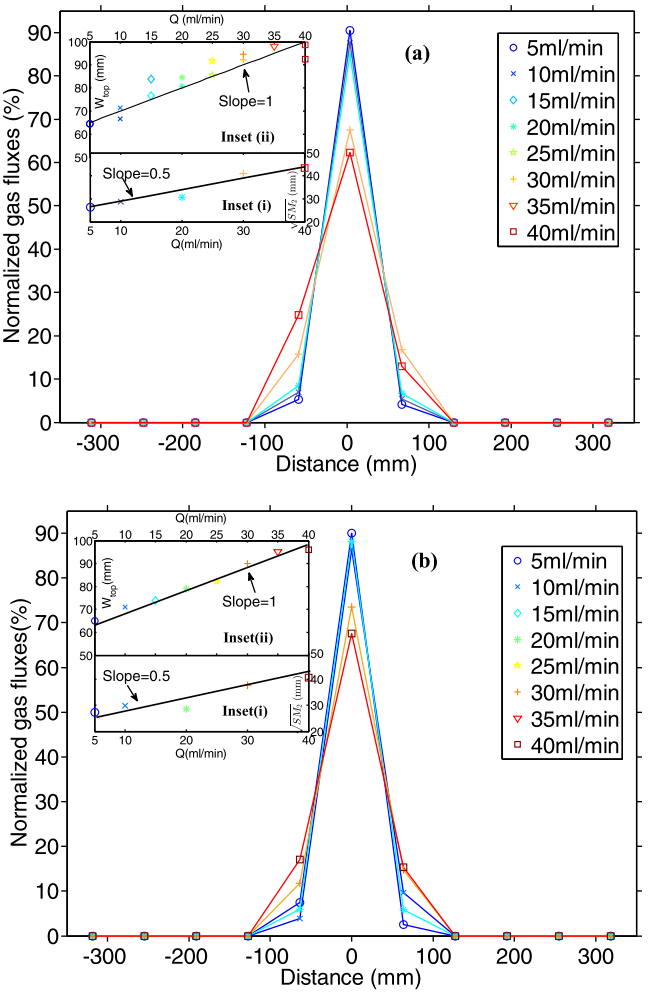

Figure 5. Normalized gas discharge rate measured at the flume top, square root of second moment of gas discharge rate variation at the flume top, $\sqrt{SM_2}$ (inset (i)), and physical width of bubble plume at the flume top, W_{top} (inset (ii)): (a) flume of $L = 700$ mm and (b) flume of $L = 500$ mm.

pressures and supersaturation levels. Discrete microbubble flow has been thought to be an important process among others for gas transport through preferential flow pathways provided by faults and fracture zones [*Etiope and Martinelli*, 2002].

Despite previous research on gas transport in porous media, not enough attention has been paid to flow of discrete and dispersed microbubbles, especially under conditions involving dynamic interactions of microbubble to microbubble, microbubble with ambient water, and microbubble with porous media. To explore the microbubble mobility in water-saturated porous media, we carried out quasi two-dimensional (2-D), lab-scale experiments to investigate the transport process of discrete microbubbles in a water-saturated transparent porous medium with a localized source of gas bubbles through a bubble diffuser at the bottom boundary. This "point" source simulates the input condition provided by air sparging or gas flow through fractures underlying the saturated soil layer. In analyzing the experimental data, we aimed to understand and quantify the advective and dispersive bubble transport behaviors. Analyses were conducted to establish the scaling relationship between the gas (bubble) release rate and various characteristic parameters of the bubble plume, such as plume tip velocity, plume width, and breakthrough time of plume front. Further analysis of momentum exchange between pore water and gas explained a pore water circulation due to bubble flow as observed in the experiments. The analysis also revealed a dependence of the mean pore water velocity on the gas release rate, which is consistent with the scaling behavior of the bubble plume.

2. Laboratory Experiments

Synthetic transparent soils are widely used for conducting porous media flow experiments [*Chen and Wada*, 1986; *Lo et al*., 2010; *Tabe et al*., 2011]. In this study, we employed transparent water-based gelbeads. Upon hydration, these gelbeads have sizes ranging from 7 to 10 mm (Figure 3). The hydrated gelbeads were then filled into two quasi-2-D transparent acrylic flumes of 700 mm × 900 mm × 30 mm ($L \times H \times \Delta h$, where L, H, and Δh are the width, height, and thickness of the flume, respectively) and 500 mm × 900 mm × 30 mm, as shown in Figures 1 and 2. The porosity (ϕ) and intrinsic permeability (κ) of packed gelbeads were measured to be approximately 0.45 and 10^{-8} m^2, respectively. The packing of the gelbeads in the flume was done through vibration and had reached a stable level of consolidation prior to the experiments.

The sodium dodecyl sulphate (SDS) surfactant was added to pore water to adjust surface tension, thus to control the size range of released bubbles [*Burns and Zhang*, 1999]. Moreover, the SDS surfactant coats a

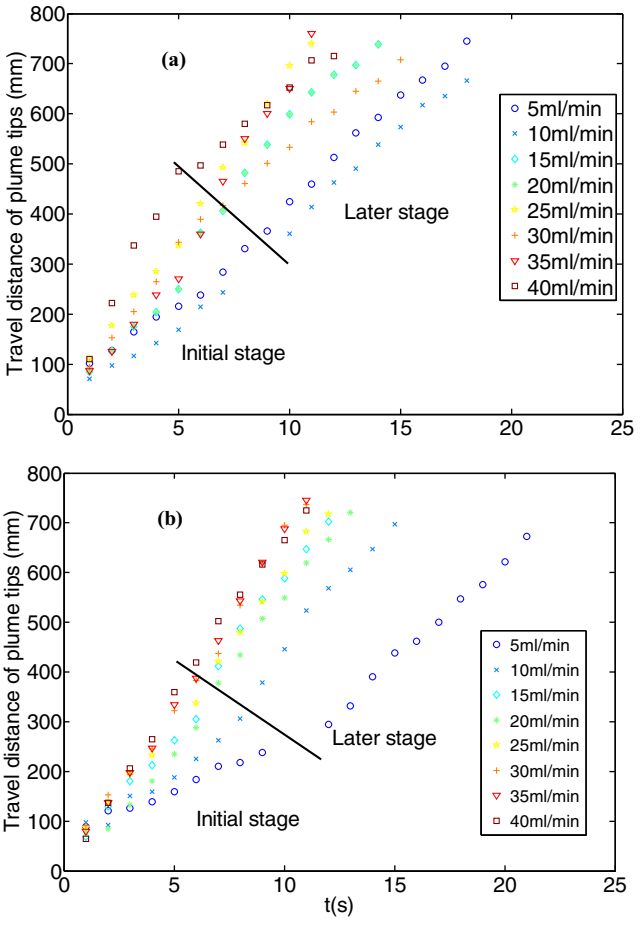

Figure 6. Temporal evolution of the travel distance of plume tip under various gas release rates, a solid black line was drawn to distinguish the initial stage and later stage: (a) flume of $L = 700$ mm and (b) flume of $L = 500$ mm.

film at the bubble interface, providing a barrier against bubble coalescence and thus maintaining bubbles separated [*Wan et al.*, 2001]. With a SDS concentration of 0.01 w/v % (weight of solute per volume of solution), the surface tension between solution and gas (nitrogen used) was measured using a Dyne gauge (Surfgauge Pty Ltd., Japan) to be 69 mN/m at 1 atm and room temperature around 20°C. Since we only applied one SDS concentration for all the experiments, the surface tension was fixed at 69 mN/m, which leads to a normal distribution of bubble size with a mean value of 300 μm and a standard deviation of 87 μm under all gas release rates applied in the study. Thus, the released bubbles are around 1 order of magnitude smaller than gelbeads (see Figure 3). This ensures that released bubbles percolate freely through the porous matrix.

Compared with gelbeads, nature soils could have particles of sizes ranging between 4 and 62 μm for clay and silt, and $\sim$1 mm for sand, which are at least an order of magnitude smaller than gelbeads. Comparably, natural microbubbles could be much smaller than the bubbles we released in the experiments, with sizes ranging from 0.1 to 100 μm [*D'Arrigo*, 1983; *Johnson and Cooke*, 1981; *Medwin*, 1970]. Therefore, our experimental setup simulates the size ratios between the pores space and gas bubbles similar to natural conditions. Bubbles (99.9% Nitrogen) were released through a bubble diffuser (diameter of ΔD=17.5 mm) placed at the center of the flume near the base (100 mm above). The gas release rate was controlled by a mass flow controller (Brooks® 4800 Series LOI), which is connected to a nitrogen gas cylinder. Bubble flow and the formed plume were recorded by a calibrated Canon Kiss X4 SLR camera at a frame rate of 1 image/s with a resolution of 5184 $\times$ 3456 pixels over the whole experiment period (Figure 2b). The camera was switched to the manual mode to maintain the same light exposure throughout the image collection, with the exposure time set to 0.02 s. The background of the experimental setup was covered with dark green sheets to minimize reflection and prevent background lights interference. The recorded images were analyzed using standard image-processing techniques (Figure 2c).

Discharge of bubbles was monitored on the flume top which was subdivided into 11 cells and sealed by an airtight lid. Each cell was connected to its own volumetric burette for measuring the gas flux associated with the bubble flow (Figure 2). The burettes, closed at the top, were connected to a shallow water tank at the bottom. The water level in the tank was kept stationary at 3 mm above the tank base. The burettes were initially filled with water. As the gas entered the burettes, it displaced the same volume of water out of the burettes into the water tank. By monitoring the water level change in each individual burette, we were able to determine the gas discharge rate for each cell over time.

In addition, ambient pore water movements were visualized using fluorescent dye tracers which were illuminated by UV light (36 W used in the study) [*Huang et al.*, 2002]. This noninvasive technique allowed us to

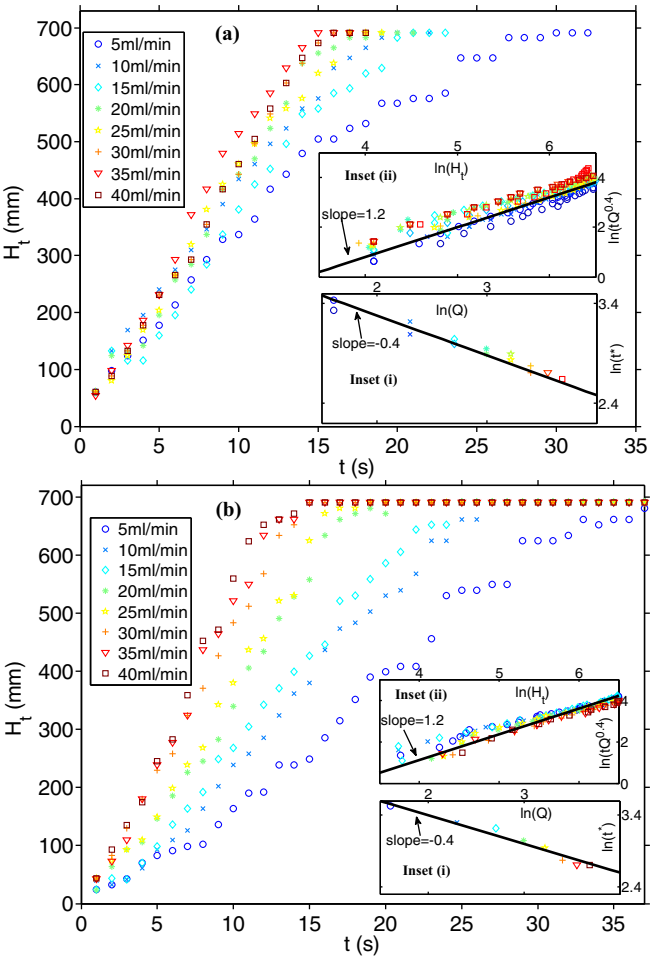

Figure 7. Temporal evolution of the bubbles plume fronts under various gas release rates, as well as ln (t^*) versus ln (Q) (inset (i)) and ln (H_t) versus ln $(tQ^{0.4})$ (inset (ii)): (a) flume of $L = 700$ mm and (b) flume of $L = 500$ mm.

quantitatively assess the velocity field of pore water. We used sodium fluorescein, an ideal conservative tracer due to its low sorption on the flume's glass wall and the gelbead surface [*Smart and Laidlaw*, 1977].

A series of experiments with different gas release rates (Q) of 5, 10, 15, 20, 25, 30, 35, and 40 mL/min were conducted. Measurements of gas discharge rate and pore water flow velocity were made for only selected cases (with gas release rates = 5, 10, 20, 30, and 40 mL/min). To discern possible boundary effects, the same series of experiments were conducted in the two flumes of different sizes, i.e., one with the flume width $L = 500$ mm and the other with $L = 700$ mm. All experiments were conducted at the atmospheric pressure and a room temperature of approximately 20°C.

3. Results and Discussion

3.1. Microbubble Transport Behaviors

A typical image of the bubble plume is shown in Figure 2b. An interconnected braided channel-like plume developed as individual bubbles freely passed through pores and throats in a zigzag/spiral motion. Trapping of bubbles and attachment of bubbles to solid surfaces or the flume walls were not visually observed. Bubbles largely moved vertically upward because of their buoyancy. Thus, there was little if any direct contact between gas and solid surfaces throughout the experiments, indicating no capillary actions involving solid surfaces [*Morrow*, 1970]. The splitting of a bubble flow path was characterized by a symmetric Y-shaped junction at the gelbead surface. This flow path splitting affected significantly the lateral spreading of the bubble plume, which behaved differently from the lateral spreading of bubbles in a flotation cell (without porous media). The latter spreading phenomenon is mainly caused by the turbulent exchange of equal size gas/liquid volume elements [*Sokolichin et al.*, 2004]. Furthermore, no oscillatory motion of the bubble plume was observed. Except for making choices at each Y-shaped junction, bubbles appeared to follow their predecessors. This kind of bubble migration along preferential flow paths also significantly differs from the conventional dispersion.

To better determine whether capillary force played a role in affecting the observed bubble flow behavior, we calculated the Bond number according to the experimental condition. The Bond number quantifies the importance of the capillary force relative to the gravitational force within the flow system, defined as $B_o = \Delta\rho g d^2/\sigma$, where d is the mean pore size, $\Delta\rho$ is the density difference between water and gas, g is the magnitude of gravitational acceleration and σ is the surface tension coefficient. The Bond number has been applied to determine gas flow patterns associated with different particle sizes. The study by *Marulanda et al.* [2000] demonstrated that above a critical Bond number, capillary trapping of the nonwetting fluid (gas) does not occur, in which case gas transport is dominated by discrete bubble flow. Under the condition of low Bond number, gas trapping controlled by the capillary force takes place, leading to channel flow [*Marulanda et al.*, 2000]. Based on the

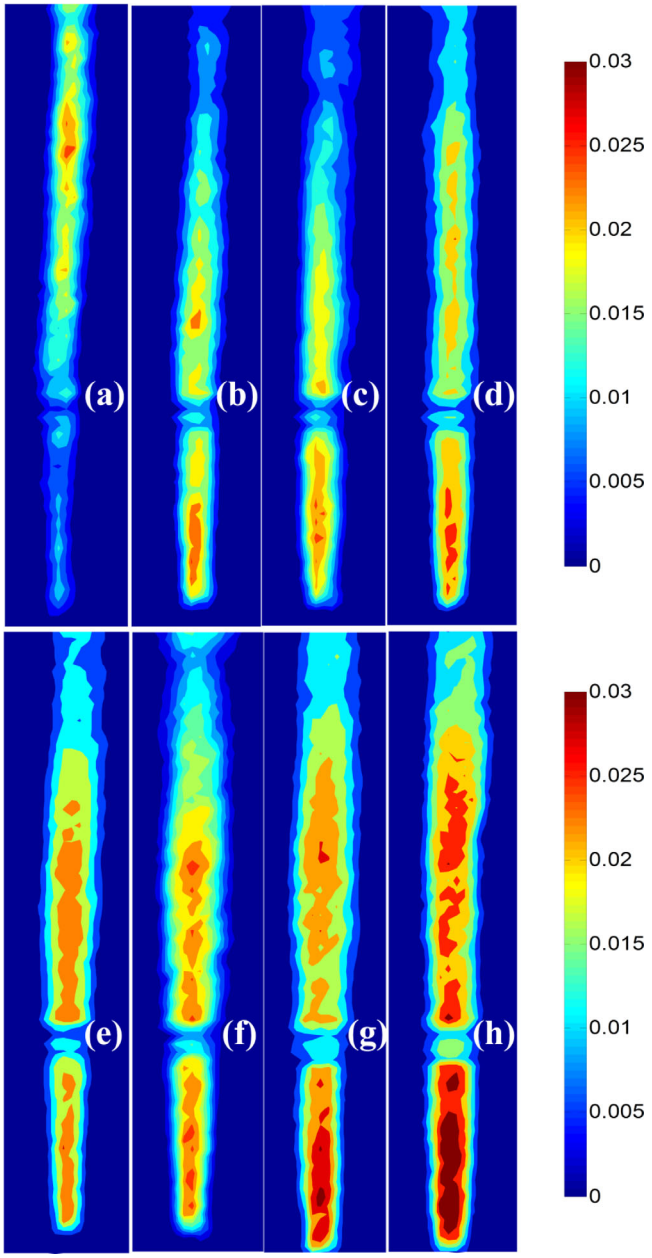

Figure 8. REV-averaged gas volume fraction distributions (after the breakthrough) at various gas release rates in the flume of $L = 700$ mm: (a) 5 mL/min, (b) 10 mL/min, (c) 15 mL/min, (d) 20 mL/min, (e) 25 mL/min, (f) 30 mL/min, (g) 35 mL/min, and (h) 40 mL/min. The gas volume fraction overall gradually increased with the gas release rate.

calculated Bond numbers according to the experimental condition, the gas flow pattern examined in the present study falls in the bubble flow regime (Figure 4). Note that the maximum and minimum Bond numbers were calculated based on the mean pore size (= 0.225 × mean particle size [*Hinedi et al.*, 1997]) and mean pore throat size (= 0.154 × mean particle size [*Hinedi et al.*, 1997]), respectively. The results from our experiments, discussed above, confirmed that the gas transport was in the bubble flow regimes under the experimental conditions.

The gas discharge from the flume top concentrated over the plume area with the maximum rate occurred at the center above the gas release point. For each experiment, we normalized measured gas discharge rates by the gas release rate to facilitate comparison of the spatial gas discharge variations for different gas release rates (Figure 5). Overall, the normalized gas discharge rate decreased with the gas release rate in the center cell but increased in the neighboring cells on both sides. This indicates that as the gas release rate increases, the lateral spreading of the bubble plume intensifies. As shown in the inset (i) of Figure 5a for $L = 700$ mm and Figure 5b for $L = 500$ mm, the square root of second spatial moment ($\sqrt{SM_2}$) of the normalized gas discharge rate varying along the flume top increases with the gas release rate correspondingly. For comparison, the variations of estimated bubble plume width at the flume top (W_{top}) are shown in the inset (ii) of Figure 5a for $L = 700$ mm and Figure 5b for $L = 500$ mm. It is evident that the slope of the $W_{top}-Q$ trendline is twice as that of the $\sqrt{SM_2}-Q$ trendline. The lateral spreading of the gas discharge followed the lateral spreading of the physical bubble plume, but with a less intensifying rate as the gas release rate increases.

Prior to breakthrough, the tip of the bubble plume moved upward and was tracked over time as shown in Figure 6a for $L = 700$ mm and Figure 6b for $L = 500$ mm, respectively. In the initial stage of the plume development (less than 5 s), a larger gas release rate produced a faster advancing plume tip. In the later stage of the plume development, the advancing of the plume tip became independent of the gas release rate, approaching a relatively constant speed estimated to be about 4 cm/s for both flumes. Assuming force balance between drag force and buoyancy force, the terminal velocity of 300 ± 89 μm bubbles can be calculated to be 3.3–9 cm/s, with a mean velocity of 6.6 cm/s. The drag coefficient, C_D, used in the calculation of drag force follows *Rodrigue* [2001],

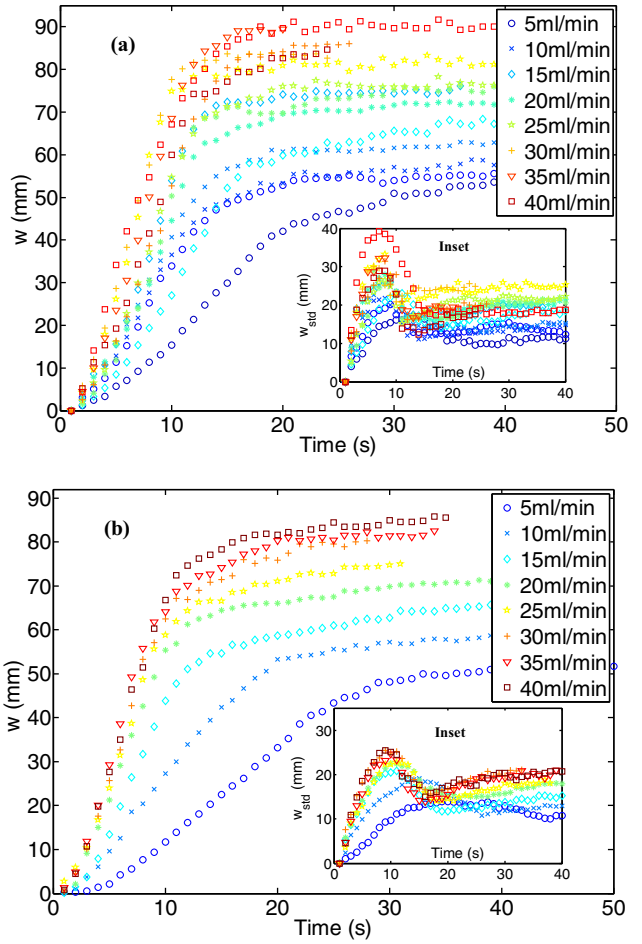

Figure 9. Evolution of the mean lateral bubble plume width and its standard deviation (shown in the inset) over time: (a) flume of $L = 700$ mm and (b) flume of $L = 500$ mm.

$$C_D = \frac{16}{\mathrm{Re}}\left[\left(\frac{1}{2}+32\theta+\frac{1}{2}\sqrt{1+128\theta}\right)^{1/3}+\left(\frac{1}{2}+32\theta-\frac{1}{2}\sqrt{1+128\theta}\right)^{1/3}+\left(0.036\left(\tfrac{128}{3}\right)^{1/9}\mathrm{Re}^{8/9}Mo^{1/9}\right)\right]^{9/4} \quad (1)$$

where $\theta=(0.018)^3\left(\frac{2}{3}\right)^{1/3}\mathrm{Re}^{8/3}Mo^{1/3}$ with $Mo=\frac{g\mu_w^4}{\rho_w\sigma^3}$ being the Morton number (μ_w is the dynamic viscosity of water, σ is the surface tension), and $\mathrm{Re}=2\frac{\rho_w vr}{\mu_w}$ (r is bubble radius and v is bubble velocity relative to water). As the plume tip's advancing velocity in the later stage is close to calculated terminal velocity, the slowdown effect on bubbles due to possible contacts with the gelbead surface was apparently limited. The SDS surfactant also seemed to have limited effect on the bubble velocity.

In addition to the plume tip, we investigated the evolution of the plume front as defined by a fixed gas volume fraction, which is equal to 20% of the maximum gas volume fraction. As shown in Figure 7a for $L = 700$ mm and Figure 7b for $L = 500$ mm, the evolution of the plume front over time exhibits an advancing speed that generally increases with the gas release rate and approaches calculated terminal velocity. Note that the gas volume fraction is defined within a Representative Elementary Volume (REV) of $8 \times 8 \times 30$ mm^3 ($D \times D \times \Delta h$, where D is the averaged gelbead size). Detailed calibration and calculation of gas volume fraction are given in the supporting information. The calibrated gas volume fraction distributions at the REV scale for various injection rates are shown in Figure 8. In general, the increment of the gas release rates resulted in higher gas volume fractions.

Similar to the plume front definition, the same fixed gas volume fraction value was also applied to define the lateral edge of the plume for measuring the lateral plume width. We calculated the mean lateral width (w) of the bubble plume as $w=\int_0^H \frac{w_{act}(h)dh}{H}$, where $w_{act}(h)$ is the bubble plume width at a height of h (distance from the bubble release position) and H is the bubble plume maximum height within the domain. The width standard deviation (w_{std}) was also calculated according to $w_{std}=\sqrt{\int_0^H \frac{(w_{act}(h)-w)^2dh}{H}}$. The mean lateral width of the bubble plume (w) and its standard deviation (w_{std}) varied over time as shown in Figure 9a for $L = 700$ mm and Figure 9b for $L = 500$ mm. Clearly, there were two distinct stages in the bubble plume development, a growing stage and a steady state stage. A larger gas release rate produced a faster growth rate, and also resulted in a shorter growing period. Moreover, w generally increased with the gas release rate. Interestingly, w_{std} showed a rapid increase followed by a sharp decline in the growing stage, and then reached a plateau. A larger gas release rate produced a higher peak value in w_{std}.

To further explore these variations, we introduced a length scale based on a characteristic width, $w^*=\sqrt[3]{Qt^*\Delta D/(\Delta h\phi)}$, and a time scale given by the time taken for the plume front to reach the flume top (i.e., breakthrough time, t^*). In the definition of w*, Q and Δh are combined (i.e., $Q/\Delta h$) to represent the

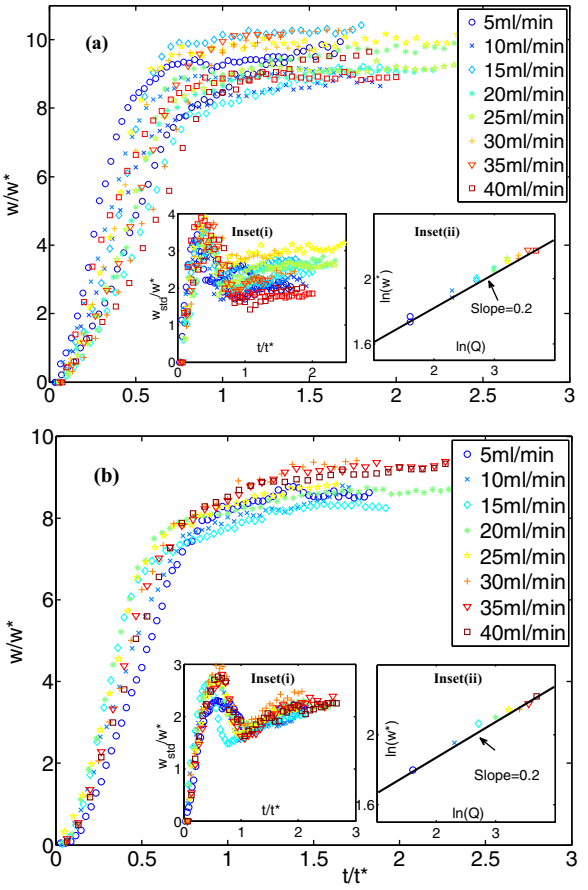

Figure 10. Plot of dimensionless bubble plume width, w/w^*, versus dimensionless time, t/t^*, as well as the dimensionless standard deviation, w_{std}/w^*, versus dimensionless time, t/t^* (inset (i)), and $\ln(w^*)$ versus $\ln(Q)$ (inset (ii)): (a) flume of $L = 700$ mm and (b) flume of $L = 500$ mm.

specific gas release rate per unit thickness. The inclusion of ΔD reflects the finite size effect of the bubble diffuser, as shown by *Selker et al.* [2007], the width of a gas plume associated with gas release from a diffuser is affected by the diameter of the diffuser. Using these scales, the mean lateral width of the bubble plume and its standard deviation as well as time were normalized/nondimensionalized. The temporal variations of the normalized bubble plume width and standard derivation for all the experiments with different gas release rates appeared to converge to relatively uniform trends (Figure 10a for $L = 700$ mm and Figure 10b for $L = 500$ mm). The scaled mean plume width (w/w^*) increased gradually to a plateau at $t/t^* = 1$. Interestingly, the temporal variation of w_{std}/w^* with the dimensionless time (t/t^*) exhibited rapid increase and decrease in the initial phase followed by a relatively constant level especially for $t/t^* \geq 1$ (inset (i) of Figure 10a for $L = 700$ mm and Figure 10b for $L = 500$ mm).

Furthermore, bubble plume profiles were investigated. The steady state bubble plume profiles are plotted in Figure 11a. Clearly, a larger gas release rate produced a wider bubble plume. The bubble plume width gradually increased with the height before reaching a constant value. Based on the same characteristic width $(w^* = \sqrt[3]{Qt^*\Delta D/(\Delta h\phi)})$, the lateral widths of the bubble plume varying with the height were also normalized/nondimensionalized. The results show clearly that the bubble plume profiles for all experiments collapse on top of each other (Figure 11b). This further demonstrates that the proposed characteristic width characterizes well the bubble plume development.

Based on the breakthrough time and total travel distance (H, the distance from the gas release point to the flume top), we can define a velocity scale (v_{bf}) as the characteristic velocity of the plume front so that the breakthrough time is given by $t^* = H/v_{bf}$. Since the advancing of the plume front is primarily driven by buoyancy force, v_{bf} can thus be estimated as an effective steady state vertical velocity of a water-gas mixture driven by its potential gradient. According to *Hubbert*'s [1940] definition of fluid potential, the derivative of this potential with respect to the vertical coordinate (in the direction of gravity) is given by ρ_{mix}/ρ_w where $\rho_{mix} = \rho_w(1-c)+\rho_g c$ is the density of the water-gas mixture with c being the bubbles/gas volume fraction, ρ_w being the water density and ρ_g being the gas density. Using Darcy's law gives, $v_{bf} = \kappa g(\rho_w - \rho_{mix})/\mu_{mix}$ [*Falta et al.*, 1989], where κ is intrinsic permeability and μ_{mix} is the effective dynamic viscosity of the mixture. According to the work of *Brown* [2000] and *Marié* [1987] and given that the gas volume fraction in the experiments was below 3%, a range comparable with natural conditions observed [*Mogollón et al.*, 2011; *Sills et al.*, 1991], the effective viscosity of water-bubble mixture changed little from the water viscosity (details in supporting information), i.e., $\mu_{mix} \approx \mu_w$. As $\rho_g << \rho_w$, the characteristic velocity (v_{bf}) of the plume front can be approximated as $v_{bf} = c\rho_w g\kappa/\mu_w$.

As a first-order approximation, c, as a characteristic scale of gas content, can be estimated as the averaged gas volume fraction within the characteristic width of the bubble plume and thus given by $c = Qt^*/(\Delta hH\phi w^*)$ with Δh being the thickness of the flume. Upon further manipulations (details of the derivation in the supporting information), one can derive the following scaling solution for the breakthrough time, i.e.,

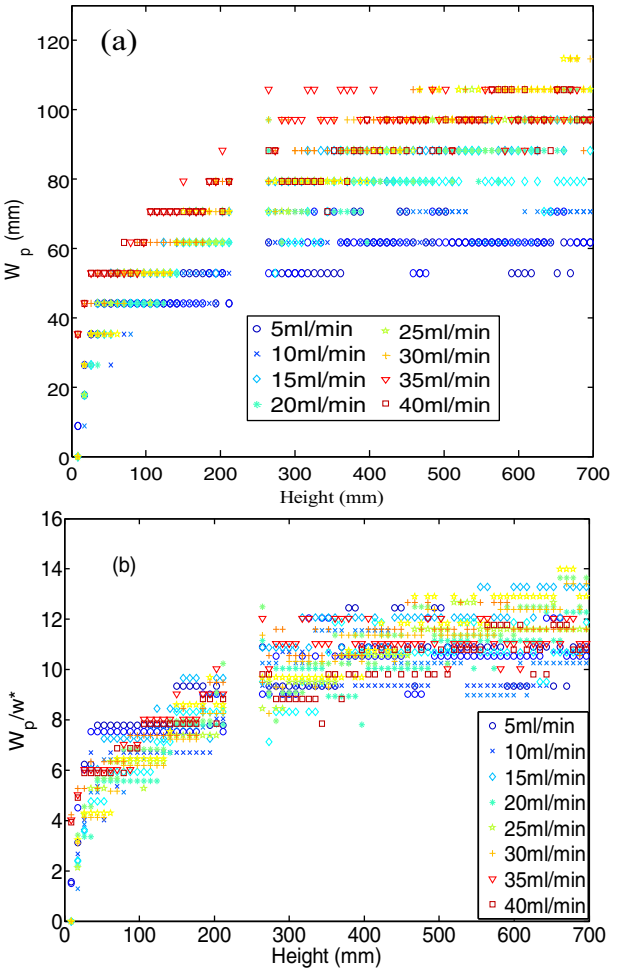

Figure 11. (a) Spatial variation of the bubble plume width, W_p, with the height at the steady state, and (b) plot of the dimensionless bubble plume width, W_p/w^*, versus the bubble plume height. The blank gap at the height between 250 and 300 mm is due to the blocking of a plexiglass beam, which was clamped around the flume surface to strengthen the support.

$$t^* = \left(\frac{\Delta h^{2/3}\phi^{2/3}\Delta D^{1/3}\mu_w}{\rho_w g\kappa}\right)^{3/5} \cdot Q^{-0.4}H^{1.2} \quad (2)$$

Alternatively c can be determined by combining $v_{bf}=c\rho_w g\kappa/\mu_w$ and $v_{bf}=\frac{Q}{w^*\phi\Delta hc}$ given by mass conservation, which leads to $c=Q^{1/3}(t^*)^{-1/6}\Delta D^{-1/6}\Delta h^{-1/3}\phi^{-1/3}(\mu_w)^{1/2}(\rho_w gk)^{-1/2}$ and consequently the same scaling solution for t^*.

According to equation (2), t^* is proportional to $Q^{-0.4}$. This was tested against and found to be in an excellent agreement with the experimental results as shown in the inset (i) of Figure 7a for $L = 700$ mm and Figure 7b for $L = 500$ mm. The scaling solution (equation (2)) also applies to the plume development ($t < t^*$) and thus $tQ^{0.4}$ is proportional to $H_t^{1.2}$ where H_t is the distance of the plume front from the release point at t ($<t^*$). This prediction was also tested and demonstrated to match well the experimental observations as shown in the inset (ii) of Figure 7a for $L = 700$ mm and Figure 7b for $L = 500$ mm. Substituting the expression of t^* (equation (2)) into w^* yields

$$w^* = Q^{0.2}H^{0.4}\left(\mu_w\Delta D^2/\Delta h\phi\rho_w g\kappa\right)^{1/5} \quad (3)$$

Equation (3) implies that the characteristic width of the bubble plume is proportional to the gas release rate with a power exponent of 0.2, a prediction consistent with the experimental results as shown in the inset (ii) of Figure 10a for $L = 700$ mm and Figure 10b for $L = 500$ mm. The results suggest that there was no lateral boundary effect on the plume development within the two flumes ($L = 700$ mm and $L = 500$ mm). This is because even the smaller flume width (500 mm) is still much larger than the bubble plume width (around 100 mm).

3.2. Microbubble-Induced Ambient Pore Water Flow

O'Hara et al. [1995] described and quantified pore water flows associated with gas ebullition by injecting gas to a tank filled with permeable sands. They manually timed the flow tracks of the dye and concluded that the pore water circulation rate is proportional to the gas injection rate. *Kong et al.* [2010b] further demonstrated that rising bubbles carried granulates along the circulation paths in water-saturated unconsolidated porous media. In the present study, we employed sodium fluorescein as passive tracers to track pore water flows. Figure 12 shows typical patterns of the pore water circulation as well as velocity fields at the steady state (after the gas breakthrough, $t > t^*$) for gas release rates of 5, 10, 20, and 30 mL/min. Circulations due to lift-up of pore water inside the bubble plume and drawdown of pore water outside the plume are clearly shown.

To examine the circulation of ambient pore water induced by the bubble flow, a momentum exchange model was established to relate the mean pore water velocity with the gas release rate. The drag force exerted on each individual bubble is given by *Clift et al.* [1978]:

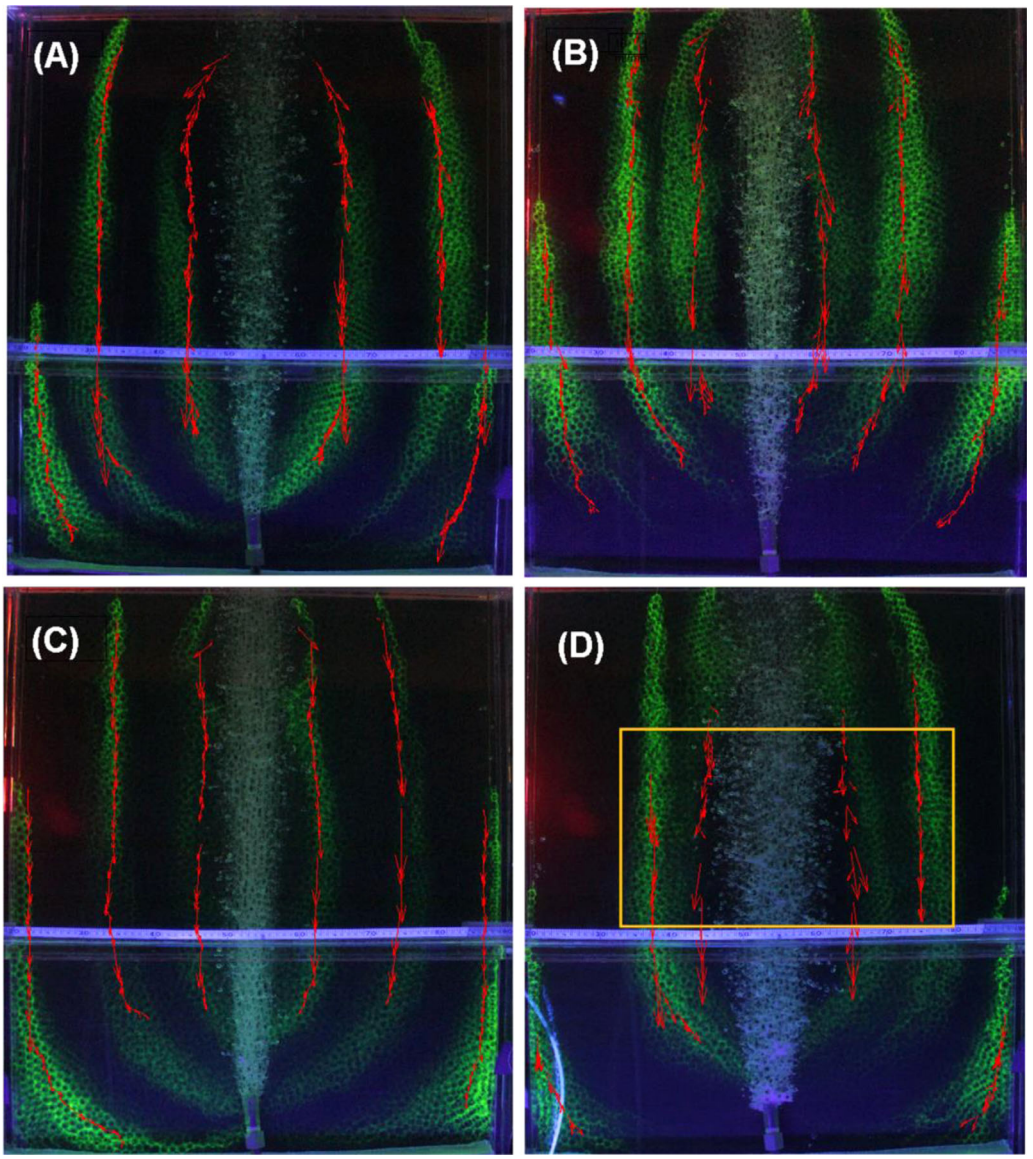

Figure 12. Flow patterns of ambient pore water visualized in the green color given by a UV illumination of the fluorescent tracers in the flume of $L = 700$ mm. The water velocity fields are illustrated in red arrows, for (a) 5 mL/min, (b) 10 mL/min, (c) 20 mL/min, and (d) 30 mL/min. The yellow rectangular box indicates the area where pore water velocities are averaged.

$$F_d = 0.5\pi r^2 C_D \rho_w v^2 \tag{4}$$

where r is the bubble radius, C_D is the drag coefficient, v is the relative velocity between bubble and water, and ρ_w is the water density.

Given the room temperature and atmospheric pressure, we have shown that Re is between 7 and 38 and $Mo \approx 2\times10^{-11}$ for a 300 ± 89 μm nitrogen bubble at its calculated terminal velocity (the largest bubble velocity that can be reached in our experimental setup). According to Figure 13, when Mo is in the order of 10^{-11} and Re is less than 40, C_D can be approximated to be [*Rodrigue*, 2001]:

$$C_D = \alpha \mathrm{Re}^{-1} \tag{5}$$

Considering the momentum exchange between the ebullient bubbles and pore water inside the plume, we have

$$F_d \cdot t^* \cdot n = M \cdot v_w \tag{6}$$

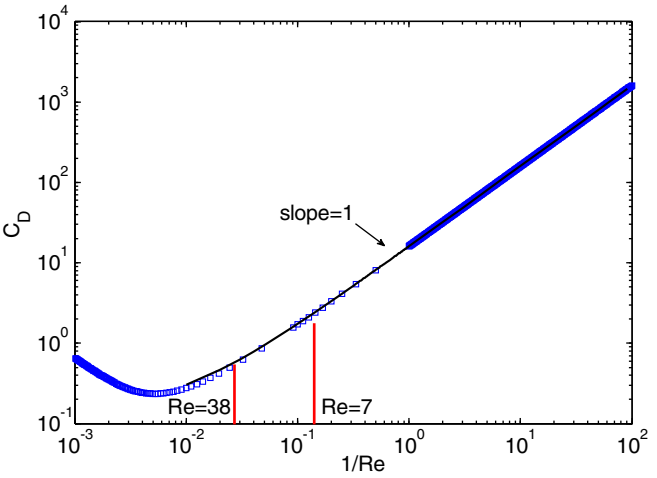

Figure 13. Based on equation (1) [*Rodrigue*, 2001], when $Mo \approx 2\times10^{-11}$, the reproduced drag coefficient versus 1/Re in a double-log plot showing a slope ~1 when Re is less than 40. Red lines are marked for Re = 7 and Re = 38, respectively.

where $n=\frac{Qt^*}{\frac{4}{3}\pi r^3}$ is the number of bubbles with a radius of r being released over the period of breakthrough time (t^*), M is the mass of water, and v_w is the average water velocity inside the bubble plume.

The relative velocity between bubble and water is given by:

$$v=v_{bf}-v_w \approx v_{bf} \tag{7}$$

Because v_{bf} is about 1 order of magnitude larger than v_w based on our experimental results, we further simplify equation (7) with $v_{bf}-v_w \approx v_{bf}$. The mass of pore water inside the bubble plume is given by:

$$M=\rho_w \Delta h H \phi w^* (1-c) \tag{8}$$

Given that the gas volume fraction is generally below 3%, we then assume $1-c \approx 1$.

We define v_s as the averaged pore water velocity over the cross-sectional area outside the bubble plume. Noting that the mass flux of pore water inside the plume equals the one outside the plume, v_w and v_s are then related to each other by:

$$v_w M = v_s M\left(\frac{L}{w*}-1\right) \tag{9}$$

After some manipulations of equations (4)–(9), we have (details of the derivation in the supporting information)

$$v_s=\frac{Q^{0.6}H^{1.2}}{r^2 L}\cdot\left(\frac{\mu_w}{\rho_w}\right)^{1.6}\left(\frac{\Delta D^{1/3}}{\Delta h \kappa g \phi}\right)^{3/5} \tag{10}$$

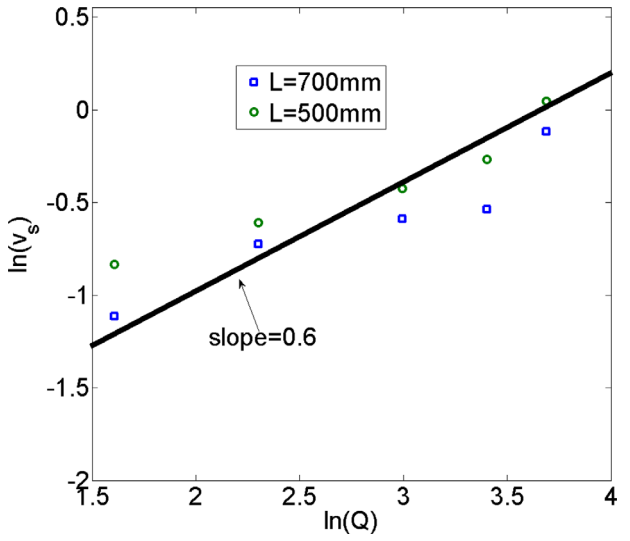

Figure 14. Averaged pore water velocity over the cross-sectional area indicated by the yellow rectangular box in Figure 12d. The averaged pore water velocities are illustrated in square and circle for flume of L =7 00 mm and flume of L = 500 mm, respectively.

Here a further simplification was made to equation (9) with $\frac{L}{w*}-1$ replaced by $\frac{L}{w*}$ since the latter value is much larger than 1. This scaling solution shows that v_s is proportional to $Q^{0.6}$, a prediction which was also tested and demonstrated to be in a good agreement with the experimental results, as shown in Figure 14, where the averaged pore water velocity (v_s) over the cross-sectional area (outside the bubble plume) is plotted versus the gas release rate. According to equation (10), v_s should increase by a factor of 1.4 when the flume width changes from 700 to 500 mm. Our experimental results showed a 1.3 times increase on average, close to the predication of the scaling solution.

4. Conclusions

Bubble flow and resulting ambient pore water circulation in a 2-D water-saturated

porous medium have been systemically and quantitatively investigated in this study. Combining the experimental results with scaling analyses, we have provided a mechanistic insight into the nature of the microbubble transport process in the porous medium through characteristic bubble plume parameters, including plume tip velocity, plume width, and breakthrough time of plume front. The characteristic width and breakthrough time of the bubble plume were shown to be proportional to the gas release rate with power exponent of 0.2 and −0.4, respectively. Circulation of ambient pore water was investigated and its cross-sectional averaged velocity was found to be proportional to the gas release rate with a power exponent of 0.6, different from the linear relationship found by *O'Hara et al* [1995].

However, we remark that the proposed scaling solutions for the bubble plume and ambient water flow are limited to the following conditions within the scope of the work performed:

1. Under conditions of extreme low gas volume fractions (approaching zero), where sparse and isolated bubbles are rising through pore space within a water-saturated porous medium, the bubble plum front velocity may be close to individual bubble velocity depending on the bubble radius but not affected by the gas volume fraction or gas release rate.
2. Under conditions of higher gas volume fraction (up to several deca-percent), the bubble plume front velocity is not only affected by the bubble size but also its volume fraction. In this regime, an effective viscosity of bubble-water mixture is often defined to count for the effect of increasing gas volume fraction [*Brown*, 2000; *Marié*, 1987]. As the gas volume fraction continues to increase, the gas transport mode may switch from the discrete bubble flow mode to channel flow mode, in which case the capillary force plays an important role.

Furthermore, the scaling solutions proposed in this study may only be applicable for discrete bubble transport in porous media with a certain range of porosity and permeability. Further studies are required to examine in detail the hydrodynamic interactions between bubble ebullition and pore water under different boundary conditions and within different types of porous media.

Nevertheless, the finding in this paper will assist the determination of influence area for the microbubble air sparging. Microbubbles have larger interfacial area, longer life time, and higher concentration. All these features increase the degree of contact between the injected air and the contaminated soil, and thus enhance oxygen transfer efficiency in groundwater bioremediation [*Li et al*., 2014b; *Tsai et al*., 2007]. Our scaling solutions for the bubble plume development will help to estimate the residence time of bubbles in porous media. Moreover, the relationship between the gas release rate and second moment of gas discharge rate variation at the flume top will advance the understanding of release of volatile organic compounds during microbubble sparging.

The findings presented here are also of particular implications for quantification of gas release rates from underground formations through preferential pathways provided by faults and fracture zones. As mentioned in section 1, field measurements of soil gas concentration anomalies (in the vadose zone below soil surface) have been used to identify these pathways under various nature conditions [*You and Zhan*, 2013]. If the width of gas distribution, w, can be inferred from the second moment of measured soil gas concentration profile, using the scaling solution derived here, we may be able to estimate the gas release rate from underlying fracture/fault zones to the soil layer. According to our results, w/w^* approaches a constant at equilibrium and w^* is proportional to the gas release rate with a power of 0.2. With the constant proportionality factor determined based on the soil layer properties, the scaling solution provides a method for estimating the gas release rate.

The scaling solutions, presented in this work, aim to capture the group behavior of the bubbles in water-saturated porous media. The analyses on the experimental results were carried out on the basis of nondimensional parameters and variables in order to explore the bubble transport mechanism in a way that is less dependent on the actual scale of the physical model. However, one should be aware of the scale effects when extrapolating the lab results immediately to the prototype in reality. Moreover, other factors, such as heterogeneity and anisotropy of porous media, can complicate the behavior of the gas (bubble) plume in reality. The work so far serves as a good starting point for further investigations to test whether the scaling solution derived in this study is scale independent or under what conditions it is applicable to real systems.

Acknowledgments
Data from the experiments and analysis can be obtained by sending a request to the corresponding author. The research project has been funded by the Australia Coal Association Research Program (ACARP C20022) and Australian Research Council Linkage Project grant (LP120100662).

References

Brooks, M. C., W. R. Wise, and M. D. Annable (1999), Fundamental changes in in situ air sparging how patterns, *Ground Water Monit. Rem.*, *19*(2), 105–113.
Brown, A. (2000), Evaluation of possible gas microseepage mechanisms, *AAPG Bull.*, *84*(11), 1775–1789.
Burns, S. E., and M. Zhang (1999), Digital image analysis to assess microbubble behavior in porous media, *J. Comput. Civ. Eng.*, *13*, 43–48.
Chen, J. D., and N. Wada (1986), Visualization of immiscible displacement in a three-dimensional transparent porous medium, *Exp. Fluids*, *4*(6), 336–338.
Chen, M.-R., R. E. Hinkley, and J. E. Killough (1996), Computed tomography imaging of air sparging in porous media, *Water Resour. Res.*, *32*(10), 3013–3024.
Clift, R., J. R. Grace, and M. E. Weber (1978), *Bubbles, Drops, and Particles*, Academic, N. Y.
D'Arrigo, J. S. (1983), Biological surfactants stabilizing natural microbubbles in aqueous media, *Adv. Colloid Interface Sci.*, *19*(4), 253–307.
De Santos, J., T. R. Melli, and L. Scriven (1991), Mechanics of gas-liquid flow in packed-bed contactors, *Annu. Rev. Fluid Mech.*, *23*(1), 233–260.
Duddridge, G. A., P. Grainger, and E. M. Durrance (1991), Fault detection using soil gas geochemistry, *Q. J. Eng. Geol. Hydrogeol.*, *24*(4), 427–435.
Elder, C. R., and C. H. Benson (1999), Air channel formation, size, spacing, and tortuosity during air sparging, *Ground Water Monit. Rem.*, *19*(3), 171–181.
Enouy, R., M. Li, M. A. Ioannidis, and A. J. A. Unger (2011), Gas exsolution and flow during supersaturated water injection in porous media: II. Column experiments and continuum modeling, *Adv. Water Resour.*, *34*(1), 15–25.
Etiope, G., and G. Martinelli (2002), Migration of carrier and trace gases in the geosphere: An overview, *Phys. Earth Planet. Inter.*, *129*(3-4), 185–204.
Falta, R. W., I. Javandel, K. Pruess, and P. A. Witherspoon (1989), Density-driven flow of gas in the unsaturated zone due to the evaporation of volatile organic compounds, *Water Resour. Res.*, *25*(10), 2159–2169.
Fleischer, R. L., and A. Mogro-Campero (1978), Mapping of integrated radon emanation for detection of long-distance migration of gases within the Earth: Techniques and principles, *J. Geophys. Res.*, *83*(B7), 3539–3549.
Fleischer, R. L., and A. Mogro-Campero (1979), Radon enhancements in the Earth: Evidence for intermittent upflows?, *Geophys. Res. Lett.*, *6*(5), 361–364.
Forsyth, P. A. (1993), A positivity preserving method for simulation of steam injection for NAPL site remediation, *Adv. Water Resour.*, *16*(6), 351–370.
Forsyth, P. A., and B. Y. Shao (1991), Numerical simulation of gas venting for NAPL site remediation, *Adv. Water Resour.*, *14*(6), 354–367.
Fry, V. A., J. S. Selker, and S. M. Gorelick (1997), Experimental investigations for trapping oxygen gas in saturated porous media for in situ bioremediation, *Water Resour. Res.*, *33*(12), 2687–2696.
Geistlinger, H., D. Lazik, G. Krauss, and H.-J. Vogel (2009), Pore-scale and continuum modeling of gas flow pattern obtained by high-resolution optical bench-scale experiments, *Water Resour. Res.*, *45*, W04423, doi:10.1029/2007WR006548.
Hinedi, Z. R., A. C. Chang, M. A. Anderson, and D. B. Borchardt (1997), Quantification of microporosity by nuclear magnetic resonance relaxation of water imbibed in porous media, *Water Resour. Res.*, *33*(12), 2697–2704.
Hu, L., X. Wu, Y. Liu, J. N. Meegoda, and S. Gao (2010), Physical modeling of air flow during air sparging remediation, *Environ. Sci. Technol.*, *44*(10), 3883–3888.
Hu, L., J. N. Meegoda, J. Du, S. Gao, and X. Wu (2011), Centrifugal study of zone of influence during air-sparging, *J. Environ. Monit.*, *13*(9), 2443–2449.
Huang, W. E., C. C. Smith, D. N. Lerner, S. F. Thornton, and A. Oram (2002), Physical modelling of solute transport in porous media: Evaluation of an imaging technique using UV excited fluorescent dye, *Water Res.*, *36*(7), 1843–1853.
Hubbert, M. K. (1940), The theory of ground-water motion, *J. Geol.*, *48*(8), 785–944.
Ji, W., A. Dahmani, D. P. Ahlfeld, J. D. Lin, and E. Hill (1993), Laboratory study of air sparging: Air flow visualization, *Ground Water Monit. Rem.*, *13*(4), 115–126.
Johnson, B. D., and R. C. Cooke (1981), Generation of stabilized microbubbles in seawater, *Science*, *213*(4504), 209–211.
Johnson, R. L., P. C. Johnson, D. B. McWhorter, R. E. Hinchee, and I. Goodman (1993), An overview of in situ air sparging, *Ground Water Monit. Rem.*, *13*(4), 127–135.
Kemski, J., R. Klingel, H. Schneiders, A. Siehl, and J. Wiegand (1992), Geological structure and geochemistry controlling radon in soil gas, *Radiat. Prot. Dosimetry*, *45*(1-4), 235–239.
Kong, X.-Z., W. Kinzelbach, and F. Stauffer (2009), Migration of air channels: An instability of air flow in mobile saturated porous media, *Chem. Eng. Sci.*, *64*(7), 1528–1535.
Kong, X.-Z., W. Kinzelbach, and F. Stauffer (2010a), Compaction and size segregation in a liquid-saturated grain packing due to pulsation effect during air injection, *Chem. Eng. Sci.*, *65*(9), 2680–2688.
Kong, X.-Z., W. Kinzelbach, and F. Stauffer (2010b), Morphodynamics during air injection into water-saturated movable spherical granulates, *Chem. Eng. Sci.*, *65*(16), 4652–4660.
Kristiansson, K., and L. Malmqvist (1984), The depth-dependence of the concentration of 222Rn in soil gas near the surface and its implication for exploration, *Geoexploration*, *22*(1), 17–41.
Li, H., L. Hu, D. Song, and F. Lin (2014b), Characteristics of micro-nano bubbles and potential application in groundwater bioremediation, *Water Environ. Res.*, *86*(9), 844–851.
Li, X., and Y. C. Yortsos (1995), Visualization and simulation of bubble growth in pore networks, *AIChE J.*, *41*(2), 214–222.
Lo, H. C., K. Tabe, M. Iskander, and S. H. Yoon (2010), A transparent water-based polymer for simulating multiphase flow, *Geotech. Test. J.*, *33*(1), 1–13.
Ma, Y., G. Yan, A. Scheuermann, D. Bringemeier, X. Z. Kong, and L. Li (2014), Size distribution measurement for densely binding bubbles via image analysis. *Experiments in Fluids*, *55*(12), 1–6.
MacElvain, R. (1969), Mechanics of gaseous ascension through a sedimentary column, in *Unconventional Methods in Exploration for Petroleum and Natural Gas*, pp. 15–28, South. Methodist Univ. Press, Dallas, Tex.
Marié, J.-L. (1987), A simple analytical formulation for microbubble drag reduction, *PhysicoChem. Hydrodyn.*, *8*(2), 213–220.
Marulanda, C., P. J. Culligan, and J. T. Germaine (2000), Centrifuge modeling of air sparging—A study of air flow through saturated porous media, *J. Hazard. Mater.*, *72*(2–3), 179–215.
McCray, J. E. (2000), Mathematical modeling of air sparging for subsurface remediation: State of the art, *J. Hazard. Mater.*, *72*(2–3), 237–263.
Medwin, H. (1970), In situ acoustic measurements of bubble populations in coastal ocean waters, *J. Geophys. Res.*, *75*(3), 599–611.

Michelsen, D. L., J. W. Smith, and J. A. Suggs (1988), Use of Colloidal gas aphrons for in-situ biodegradation of contaminated ground water, in *Conference Proceedings: Land Disposal, Remedial Action, Incineration and Treatment of Hazardous Waste*, US EPA, edited by J. F. Martin, and E. F. Harris, pp. 203–217, Cincinnati, Ohio.

Mogollón, J. M., A. W. Dale, I. L'Heureux, and P. Regnier (2011), Impact of seasonal temperature and pressure changes on methane gas production, dissolution, and transport in unfractured sediments, *J. Geophys. Res.*, *116*, G03031, doi:10.1029/2010JG001592.

Montgomery, S. L., and M. F. Morea (2001), Antelope shale (Monterey Formation), Buena Vista Hills field: Advanced reservoir characterization to evaluate CO_2 injection for enhanced oil recovery, *AAPG Bull.*, *85*(4), 561–586.

Moore, T. A. (2012), Coalbed methane: A review, *Int. J. Coal Geol.*, *101*, 36–81.

Morrow, N. R. (1970), Physics and thermodynamics of capillary action in porous media, *Ind. Eng. Chem.*, *62*(6), 32–56.

Nelson, L., J. Barker, T. Li, N. Thomson, M. Ioannidis, and J. Chatzis (2009), A field trial to assess the performance of CO_2-supersaturated water injection for residual volatile LNAPL recovery, *J. Contam. Hydrol.*, *109*(1–4), 82–90.

O'Hara, S. C. M., P. R. Dando, U. Schuster, A. Bennis, J. D. Boyle, F. T. W. Chui, T. V. J. Hatherell, S. J. Niven, and L. J. Taylor (1995), Gas seep induced interstitial water circulation: Observations and environmental implications, *Cont. Shelf Res.*, *15*(8), 931–948.

Osborn, S. G., A. Vengosh, N. R. Warner, and R. B. Jackson (2011), Methane contamination of drinking water accompanying gas-well drilling and hydraulic fracturing, *Proc. Natl. Acad. Sci. U. S. A.*, *108*(20), 8172–8176.

Pleasant, S., A. O'Donnell, J. Powell, P. Jain, and T. Townsend (2014), Evaluation of air sparging and vadose zone aeration for remediation of iron and manganese-impacted groundwater at a closed municipal landfill, *Sci. Total Environ.*, *485–486*, 31–40.

Rebata-Landa, V., and J. Santamarina (2012), Mechanical effects of biogenic nitrogen gas bubbles in soils, *J. Geotech. Geoenviron. Eng.*, *138*(2), 128–137.

Rodrigue, D. (2001), Drag coefficient—Reynolds number transition for gas bubbles rising steadily in viscous fluids, *Can. J. Chem. Eng.*, *79*(1), 119–123.

Santos, I. R., B. D. Eyre, and M. Huettel (2012), The driving forces of porewater and groundwater flow in permeable coastal sediments: A review, *Estuarine Coastal Shelf Sci.*, *98*, 1–15.

Saunders, D. F., K. R. Burson, and C. K. Thompson (1999), Model for hydrocarbon microseepage and related near-surface alterations, *AAPG Bull.*, *83*, 170–185.

Selker, J., M. Niemet, N. McDuffie, S. Gorelick, and J.-Y. Parlange (2007), The local geometry of gas injection into saturated homogeneous porous media, *Transp. Porous Media*, *68*(1), 107–127.

Sills, G. C., S. J. Wheeler, S. D. Thomas, and T. N. Gardner (1991), Behaviour of offshore soils containing gas bubbles, *Geotechnique*, *41*(2), 227–241.

Smart, P. L., and I. M. S. Laidlaw (1977), An evaluation of some fluorescent dyes for water tracing, *Water Resour. Res.*, *13*(1), 15–33.

Sokolichin, A., G. Eigenberger, and A. Lapin (2004), Simulation of buoyancy driven bubbly flow: Established simplifications and open questions, *AIChE J.*, *50*(1), 24–45.

Tabe, K., M. Iskander, and S. Honma (2011), Transparent aquabeads to visualize flow in porous material, *Adv. Mater. Res.*, *239*, 2602–2605.

Thomson, N. R., and R. L. Johnson (2000), Air distribution during in situ air sparging: An overview of mathematical modeling, *J. Hazard. Mater.*, *72*(2–3), 265–282.

Tsai, Y.-J., Y.-C. Kuo, and T.-C. Chen (2007), Groundwater remediation using a novel micro-bubble sparging method, *J. Environ. Eng. Manage.*, *17*(2), 151–155.

Wan, J., S. Veerapaneni, F. Gadelle, and T. K. Tokunaga (2001), Generation of stable microbubbles and their transport through porous media, *Water Resour. Res.*, *37*(5), 1173–1182.

Weinlich, F., J. Tesar, S. Weise, K. Brauer, and H. Kampf (1998), Gas flux distribution in mineral springs and tectonic structure in the western Eger Rift, *J. Geosci.*, *43*(1-2), 91–110.

You, K., and H. Zhan (2013), Comparisons of diffusive and advective fluxes of gas phase volatile organic compounds (VOCs) in unsaturated zones under natural conditions, *Adv. Water Resour.*, *52*, 221–231.

Zhao, W., and M. A. Ioannidis (2011), Gas exsolution and flow during supersaturated water injection in porous media: I. Pore network modeling, *Adv. Water Resour.*, *34*(1), 2–14.